PHYSICAL REVIEW E **104**, 024218 (2021)

Effect of gravity on synchronization of two coupled buoyancy-induced turbulent flames

Takumi Tokami,[1] Masaharu Toyoda,[1] Takaya Miyano,[2] Isao T. Tokuda,[2] and Hiroshi Gotoda[1,*]
[1]*Department of Mechanical Engineering, Tokyo University of Science, 6-3-1 Niijuku, Katsushika, Tokyo 125-8585, Japan*
[2]*Department of Mechanical Engineering, Ritsumeikan University, 1-1-1 Nojihigashi, Kusatsu, Shiga 525-8577, Japan*

(Received 4 January 2021; revised 8 May 2021; accepted 15 June 2021; published 24 August 2021)

We study the effect of gravity on the synchronization of two coupled buoyancy-induced turbulent flames by recurrence-based analysis and machine learning. A significant change from nearly complete synchronization in the near field to partial synchronization appears in the far field under low gravity. The synchronized state is gradually lost with increasing gravity level. These results are clearly identified from cross recurrence plots and symbolic recurrence plots and by reservoir computing.

DOI: 10.1103/PhysRevE.104.024218

I. INTRODUCTION

A mutual interplay among the convective motion of fluid, the heat-mass diffusion, and rapid chemical reactions, gives rise to a rich variety of flame front instabilities in a combusting flow. A whole flow field forming an open diffusion flame with low flow velocity of fuel is predominantly composed of two gases: combustion products behind the flame front and surrounding quiescent air. A large difference in density between the two gases exposed to gravity triggers an upward buoyant flow. A buoyancy-induced toroidal vortex is formed in the interface between the two gases owing to a modified Kelvin-Helmholtz-type hydrodynamic instability mechanism [1–3]. The interference of the traveling toroidal vortex with the flame front results in a substantial distortion of the flame front configuration owing to the unstable density stratification associated with the Rayleigh-Taylor instability mechanism [4], leading to self-excited periodic flame front oscillations with low frequency and large amplitude. These physical processes significantly affect the generation and growth of a buoyancy-induced turbulent diffusion flame [5]. Thus far, the instantaneous and time-averaged flow velocity [6–12], vorticity [11,13,14], temperature [4,7–9,11–15], and turbulent statistics [7–9,12,16] in buoyant plumes, buoyant jet diffusion flames, and pool fires have been extensively studied in addition to the empirical correlation between the dominant oscillation frequency of the flame front and dimensionless numbers, such as the Strouhal number, the Froude number, and the Richardson number [4,6,14,15,17–22].

Nonlinear time series analysis based on the theories of dynamical systems and symbolic dynamics has become a promising tool for revealing the nonlinear dynamics in complex combustion phenomena [23–29]. We have recently studied the spatiotemporal dynamics of flow velocity and temperature fields during a buoyancy-induced turbulent fire under normal gravity by complexity analysis [30] in terms of symbolic dynamics [31,32]. The possible presence of two important dynamics has been identified: one is low-dimensional chaos in the near field dominated by the unstable motion of an organized toroidal vortex, and the other is high-dimensional chaos in the far field forming a well-developed turbulent plume [31,32]. The gravitational term (baroclinic torque term) in the vorticity equation has a significant impact on the formation of low-dimensional chaos (high-dimensional chaos) [33].

Synchronization phenomena, which emerge upon the coupling of nonlinear oscillators, have been observed in various fields involving physics, chemistry, electronics, and biology [34–36]. The quest for such phenomena has raised much interest of researchers in the field of nonlinear science. An elucidation of the synchronization between multiple diffusion flames is one of the key challenges associated with the systematization of complex combustion and fire dynamics [37–45]. We have studied synchronization phenomena in two coupled turbulent fires under normal gravity [46]. When two fire sources are located close to each other, their synchronized state occurs in the near field, whereas it vanishes in the far field, regardless of the distance between the two fire sources. This is clearly identified from the mutual information, the recurrence rate, and the mean diagonal line length in cross recurrence plots (CRPs) [47,48]. Our next interest is the exploration of the synchronization phenomena in two coupled buoyancy-induced turbulent flames under various gravity levels.

The purpose of this paper is to clarify the effect of gravity on the synchronization of two coupled turbulent diffusion flames by recurrence-based analysis and supervised machine learning. CRPs [47,48] are useful for detecting synchronization between two coupled systems. Symbolic recurrence plots (SRPs) [48,49], which are recurrence plots incorporating rank-order patterns in time series, can quantify the degree of similarity between two dynamical states in relation to synchronization phenomena [50]. Recurrence-based analysis is useful for investigating the nonlinear correlation between two dynamic behaviors. In this paper, we estimate the recurrence rate of both recurrence plots to evaluate the synchronized states. Supervised machine learning has been widely used for solving various problems in physics. Reservoir computing,

---

[*] Corresponding author: gotoda@rs.tus.ac.jp

which is a type of supervised machine learning, is a subclass of recurrent neural networks, and has shown good performance in predicting the short-term behavior of spatiotemporal chaos [51,52]. Tokami *et al.* [33] have elucidated that on-off intermittent behavior between turbulent combustion products and nonturbulent ambient occurs in the region of high-entropy transfer from temperature fluctuations to flow velocity fluctuations. This was clearly explained by the predictability of flow velocity fluctuations obtained by reservoir computing. An important motivation in this paper is to examine whether reservoir computing is helpful for clarifying the synchronized state in coupled turbulent flow systems. In this paper, we show the applicability of reservoir computing to a discussion of the degree of synchronization between two coupled turbulent flames.

This paper is organized as follows: A brief description of the numerical simulation and the analytical methods based on the theories of dynamical systems and symbolic dynamics is provided in Sec. II, including the supervised machine learning approach. Numerical results and discussion are given in Sec. III. Finally, we give a summary in Sec. IV.

II. NUMERICAL SIMULATION AND ANALYTICAL METHODS

A. Numerical simulation

We numerically obtain the spatiotemporal structure of buoyancy-induced turbulent diffusion flames by employing an open-source numerical simulation code [53,54]. The following governing equations (i.e., the mass conservation equation, momentum conservation equation, energy conservation equation, and chemical species equations) are numerically solved in this paper:

$$\frac{\partial \rho}{\partial t} + \nabla \cdot (\rho \mathbf{u}) = 0, \tag{1}$$

$$\rho\left(\frac{\partial \mathbf{u}}{\partial t} + (\mathbf{u} \cdot \nabla)\mathbf{u}\right) + \nabla p = \rho \mathbf{g} + \nabla \cdot \tau_v, \tag{2}$$

$$\frac{\partial}{\partial t}(\rho h) + \nabla \cdot (\rho h \mathbf{u}) = \frac{Dp}{Dt} + \dot{q}''' - \nabla \cdot \mathbf{q}_r + \nabla \cdot (\lambda \nabla T) + \nabla \cdot \left(\rho \sum_l h_l D_l \nabla Y_l\right), \tag{3}$$

$$\frac{\partial}{\partial t}(\rho Y_l) + \nabla \cdot (\rho Y_l \mathbf{u}) = \nabla \cdot (\rho D_l \nabla Y_l) + \dot{m}_l'''. \tag{4}$$

Here, ρ is the density, t is the time, $\mathbf{u}$ $[=(u, v, w)]$ is the flow velocity vector, Y_l is the mass fraction of chemical species l, D_l is the diffusivity of chemical species l, $\dot{m}_l'''$ is the production rate of chemical species l per unit volume, p is the pressure, $\mathbf{g}$ is the gravitational acceleration vector, τ_v is the viscous stress tensor, h $(=T\sum_{l=1}^{N_s} c_{p,l} Y_l$, where $c_{p,l}$ is the specific heat capacity of chemical species l and N_s is the number of chemical species) is the enthalpy, $\dot{q}'''$ is the heat release rate per unit volume, $\mathbf{q}_r$ is the radiative heat flux vector, λ is the thermal conductivity, T is the temperature, and h_l is the enthalpy of chemical species l. In this paper, we consider CH_4, O_2, N_2, CO_2, and H_2O as chemical species, and a global single-step irreversible chemical reaction with $N_s = 5$ under a low-Mach-number flow [53]. The Smagorinsky model is adopted for the viscous stress in the momentum conservation equation. $\dot{q}'''$ is approximated by a mixture fraction combustion model, assuming that the mass fraction of all the species is described by the mixture fraction. The second-order finite differences and an explicit second-order predictor-corrector scheme are adopted for spatial derivatives and temporal derivatives in the governing equations, respectively. The radiative term in the energy conservation equation is solved using the finite volume method. We employ a nonslip and adiabatic boundary condition for the walls of the flame source with a height of 0.01 m and the floor corresponding to the bottom plane outside the flame source. The top and vertical boundaries of the computational domain are set to be open, allowing free inflow or outflow.

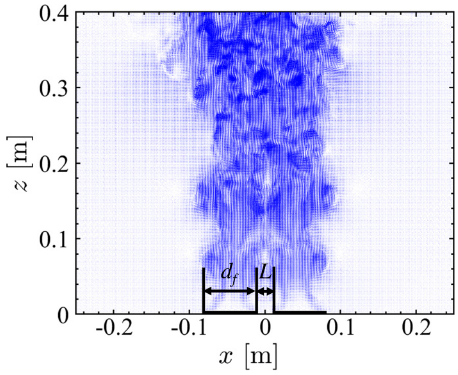

FIG. 1. Instantaneous flow velocity field on the x-z plane at $y = 0$ mm in two coupled turbulent diffusion flames under normal gravity.

In accordance with the numerical study conducted by Xin *et al.* [11], we set the computational domain in the x, y, and z directions to 0.5, 0.3, and 0.4 m, respectively. The total number of cells for a uniform grid size of 2 mm is 7500000, and the time resolution in the numerical simulation is 0.1 ms. Note that the grid size and the time resolution in the numerical simulation are the same as those in the previous study [11]. The gaseous fuel CH_4 is supplied from a center area with a square shape, where the side length of the center area d_f is 71 mm. The mean axial flow velocity w_f of CH_4 from the flame source is estimated to be 0.023 m/s. As shown in Fig. 1, the normalized distance between two flame sources L^* $(=L/d_f$, where L is the distance between the two sources) is set to 0.3 in this paper. We consider various gravity levels from low $(G = 0.4)$ to high $(G = 2)$, where G $(=g_a/g)$ is the gravity level, g_a is the gravitational acceleration in the computational domain, and g is the gravitational acceleration under normal gravity.

We apply CRPs, SRPs, and reservoir computing to the analysis of time variations in the second-order moment of flow velocity fluctuations along the z direction M_w $(= \langle |w(x, 0, z) - \langle w(x, 0, z)\rangle_x|^2\rangle_x)$, where $\langle w(x, 0, z)\rangle$ denotes the mean value over the region corresponding to d_f. We analyze the temporal evolutions in M_w over 2.0 s $(N = 20\,001$, where N is the total number of data points of $M_w)$ under a statistical stationary state after discarding the initial transient state during the numerical simulation. Note that in our preliminary test, we confirmed that the length of the time series does not affect the permutation entropy [55] for all the gravity levels.

B. Analytical methods

Recurrence plots, which show the recurrence patterns of the trajectory in phase space, have been widely utilized to study the changes in a dynamical state. CRPs [47] have been proposed as a bivariate extension of recurrence plots to capture the similarity of the evolution of two dynamical states. The central idea of this approach is the comparison of recurrence patterns in the trajectories of two time series embedded in the same phase space. In this paper, we examine the interrelationships between temporal evolutions of M_{w1} for the left-hand flame source and M_{w2} for the right-hand flame source. The cross recurrence matrix consists of $C_{R,ij}$ $\{= \Theta[\epsilon - \|\mathbf{M}_{w1}(t_i) - \mathbf{M}_{w2}(t_j)\|]\}$. Here, Θ is the Heaviside function, ϵ is the threshold, $\| \cdot \|$ is the Euclidean norm, $\mathbf{M}_{w1}(t_i)=[M_{w1}(t_i), M_{w1}(t_{i+\tau}), \ldots, M_{w1}(t_{i+(D-1)\tau})]$, $\mathbf{M}_{w2}(t_j) = [M_{w2}(t_j), M_{w2}(t_{j+\tau}), \ldots, M_{w2}(t_{j+(D-1)\tau})]$, and τ is the embedding delay time. The density of recurrence points R_R in CRPs enables us to quantify the degree of synchronization between the two time series. R_R is defined as

$$R_R = \frac{1}{N_t - |\tau_l|} \sum_{i=1}^{N_t - |\tau_l|} C_{R,ij}. \tag{5}$$

Here, N_t $[=N - (D-1)\tau)]$ is the total number of points in the phase space, τ_l is the time distance from the main diagonal line, and j is set to $i + \tau_l$. τ_l is set to zero for the estimation of R_R. Note that ϵ is determined so as to satisfy the recurrence point density [48] r_d $[=\sum_{\tau_l=0}^{N_t}(N_t - |\tau_l|)R_R/N_t^2] = 0.05$ (see the Appendix). In accordance with the prescription of Kennel *et al.* [56], D is set to 5 (see the Appendix). τ is set to the time when the mutual information [57] first takes a minimum.

SRPs [48,49] incorporating the rank order patterns in time series are also useful for discussing the similarity of two dynamical states in terms of synchronization [50]. We apply SRPs to M_{w1} and M_{w2}. The symbolic recurrence matrix consists of $S_{R,ij}$ (equals unity when $\pi^D_{M_{w1}}(t_i) = \pi^D_{M_{w2}}(t_j)$, whereas zero when $\pi^D_{M_{w1}}(t_i) \neq \pi^D_{M_{w2}}(t_j)$. Here, $\pi^D_{M_{w1}}(t_i)[\pi^D_{M_{w2}}(t_j)]$ is the rank order pattern of $M_{w1}(M_{w2})$, and j is set to $i + \tau_l$). Note that the D! possible permutations of D successive data points in sampled time series at intervals of τ, which are indexed as π^D, represent the rank order patterns. In this paper, we estimate S_R to quantify the degree of synchronization between M_{w1} and M_{w2},

$$S_R = \frac{1}{N_t - |\tau_l|} \sum_{i=1}^{N_t - |\tau_l|} S_{R,ij}. \tag{6}$$

Here, S_R represents the density of recurrence points in SRPs and significantly increases as two dynamic behaviors become synchronized. In this paper, we change τ_l to study the lagged synchronization.

Reservoir computing has been recognized as one of the sophisticated and promising model-free predictors [52]. A previous study revealed that an echo state network is effective for short-term prediction of hyperchaotic time series generated by a hydrodynamical model simulating turbulent thermal convection [58]. We have recently shown the importance of reservoir computing for elucidating the dynamical state in the near field during a buoyancy-induced turbulent fire [33]. In this paper, we introduce reservoir computing to discuss the relationship between the predictability of flow velocity fluctuations and the synchronized state of two coupled turbulent flames. The estimation of the predictability of the responding variable from the driving variable is important for examining mutual synchronization between two coupled turbulent diffusion flames, where we consider M_{w1} and M_{w2} to be the driving variable and the responding variable, respectively. The reservoir computer comprises an input layer, a reservoir, and an output layer. We use the echo state networks as the simplest form of the reservoir. The reservoir state $\mathbf{r}(t_i)$ [59,60] during the training phase of the reservoir computer is updated as follows:

$$\mathbf{r}(t_i + \Delta t) = (1 - \alpha)\mathbf{r}(t_i) + \alpha\phi[\mathbf{r}(t_i), \mathbf{u}(t_i)], \tag{7}$$

$$\phi[\mathbf{r}(t_i), \mathbf{u}(t_i)] = \tanh\left[\mathbf{W}\mathbf{r}(t_i) + \mathbf{W}_{\text{in}}\begin{pmatrix} 1 \\ \mathbf{u}(t_i) \end{pmatrix}\right]. \tag{8}$$

Here, $\mathbf{u}(t_i) = [M_{w1}(t_i); M_{w2}(t_i)]$, $\mathbf{W}_{\text{in}}$ is the weighted matrix between the input layer and the reservoir, and $\mathbf{W}$ is the $D_r \times D_r$ adjacency matrix of the reservoir network. We use the first 1 s (10 001 points) of $M_{w1}(t_i)$ and $M_{w2}(t_i)$ for training the reservoir computer. Uniform random numbers, which range from -1 to 1, are given to the matrix elements of $\mathbf{W}$ as the initial state of the weighted matrix. Similar to in our recent study [33], D_r is set to 1000, and $\mathbf{W}$ includes a sparse random matrix with 200 000 nonzero components. The leakage rate α corresponding to the update speed of the reservoir dynamics is varied from 0 to 1 [61]. After updating the reservoir, the output vector $\mathbf{v}(t_i)$ [59,60] is obtained by linear mapping from $\mathbf{u}(t_i)$ and $\mathbf{r}(t_i)$,

$$\mathbf{v}(t_i) = \mathbf{W}_{\text{out}}\begin{pmatrix} 1 \\ \mathbf{u}(t_i) \\ \mathbf{r}(t_i) \end{pmatrix}, \tag{9}$$

where $\mathbf{W}_{\text{out}}$ is the weighted matrix between the output layer and the reservoir. This process is repeated for the learning steps, where $0 \leqslant i \leqslant n$. Tikhonov-Arsenin regularization [62] is adopted to optimize $\mathbf{W}_{\text{out}}$ to minimize the error between $\mathbf{v}(t_i)$ and the training data $\mathbf{v}_d(t_i)$,

$$\mathbf{W}_{\text{out}} = \mathbf{v}_d\mathbf{s}^T(\mathbf{s}\mathbf{s}^T + \beta\mathbf{I})^{-1}, \tag{10}$$

$$\mathbf{s} = \begin{pmatrix} 1 & 1 & \cdots & 1 \\ \mathbf{u}(t_0) & \mathbf{u}(t_0 + \Delta t) & \cdots & \mathbf{u}(t_n) \\ \mathbf{r}(t_0) & \mathbf{r}(t_0 + \Delta t) & \cdots & \mathbf{r}(t_n) \end{pmatrix}. \tag{11}$$

Here, β is the regularization coefficient $(=1 \times 10^{-6})$, $\mathbf{I}$ is the identity matrix, Δt is 0.1 ms, and $n = 10\,000$. We set $\mathbf{v}_d(t_i) = [M_{w1}(t_i + \Delta t); M_{w2}(t_i + \Delta t)]$. We adopt $\mathbf{u}(t_i) = [M_{w1}(t_i); M_{w2,\text{predict}}(t_i)]$ for the prediction steps and finally obtain $\mathbf{v}(t_i) = [M_{w1,\text{predict}}(t_i + \Delta t); M_{w2,\text{predict}}(t_i + \Delta t)]$, where the number of predicted data points is 9001, corresponding to 0.9 s.

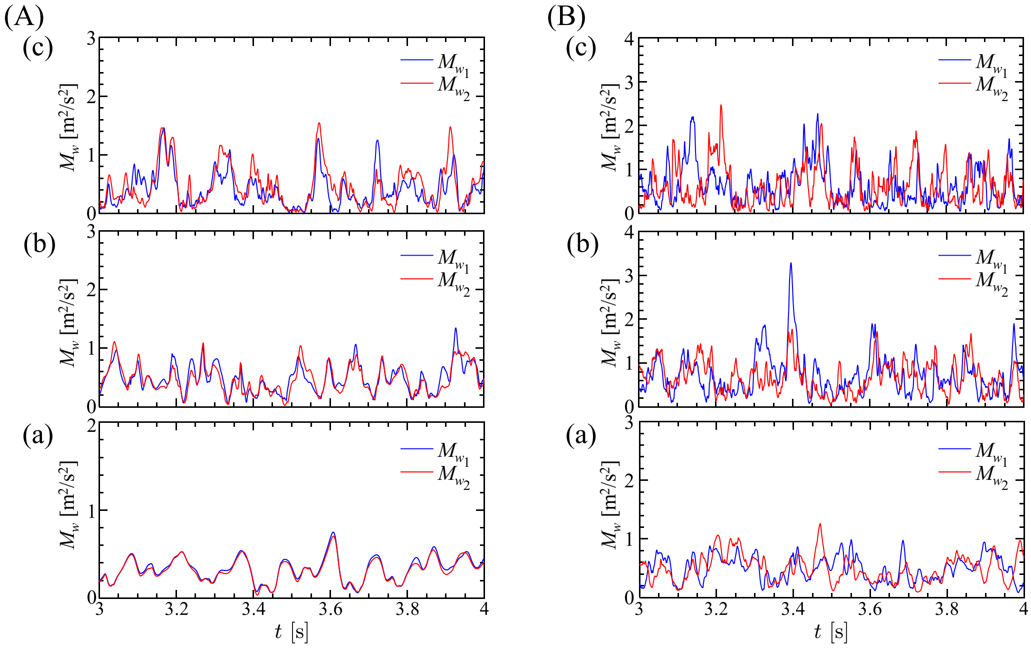

FIG. 2. Time variations in the second-order moment of flow velocity fluctuations along z axis M_{w1} and M_{w2} at different locations z under (A) low gravity ($G = 0.7$) and (B) high gravity ($G = 1.5$). (a) $z = 0.1$ m, (b) $z = 0.2$ m, and (c) $z = 0.3$ m.

III. RESULTS AND DISCUSSION

Figure 2 shows time variations in M_{w1} and M_{w2} at different locations z under low gravity ($G = 0.7$) and high gravity ($G = 1.5$). We clearly observe the coincidence of M_{w1} and M_{w2} at $z = 0.1$ m under low gravity, indicating the emergence of nearly complete synchronization. Here, $z = 0.1$ m corresponds to the near field. The synchronized state starts to be lost at $z = 0.2$ m and becomes a partially synchronized state at $z = 0.3$ m. These synchronized states vanish at each z under high gravity. The variation in R_R at different z is shown in Fig. 3 as a function of G. R_R takes a value of unity at $z \leqslant 0.16$ m under a low gravity of $G = 0.7$, indicating the formation of a completely synchronized state in the near field. It monotonically decreases with increasing z. A nearly completely synchronized state is formed at $z \leqslant 0.1$ m under normal gravity ($G = 1$). R_R at $G = 1$ notably decreases with increasing z, compared with that at $G = 0.7$. Under the high gravity of $G = 1.5$, the nearly completely synchronized state vanishes in the near field and becomes a nonsynchronized state in the far field. Takagi and Gotoda [63] clearly showed that for a buoyancy-induced turbulent fire with a flame source larger than that in this paper, the formation region of high-dimensional deterministic chaos is enhanced with increasing gravity level. The extension of the formation region is significantly associated with the nonsynchronized state in two coupled turbulent diffusion flames. One of the authors has recently studied the synchronized state of thermoacoustic combustion dynamics in a gas-turbine model combustor using the maximal information coefficient as a class of the correlation coefficient in terms of information theory [64]. We here adopt it for M_{w1} and M_{w2}. The variation in the maximal information coefficient C_M as a function of G for different z is shown in Fig. 4. C_M nearly takes a value of unity at $z < 0.16$ m under $G = 0.7$, indicating the formation of a completely synchronized state. A nearly completely synchronized state is formed at $z < 0.1$ m under $G = 1$ and vanishes under $G = 1.5$. The distribution of C_M

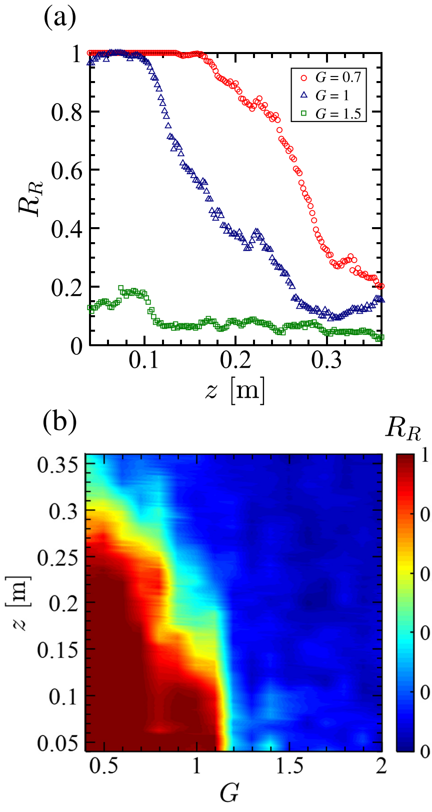

FIG. 3. (a) Variation in the recurrence rate R_R of the CRPs at different locations z for gravity levels $G = 0.7$, 1, and 1.5. (b) Surface plot of R_R as a function of G at different z.

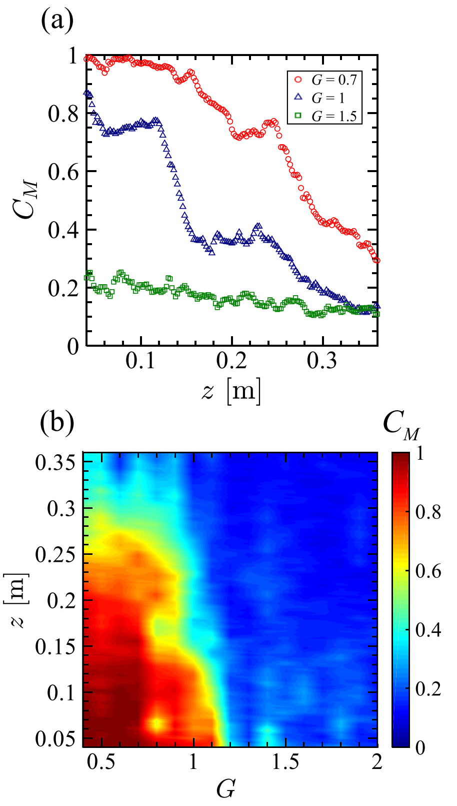

FIG. 4. (a) Variation in the maximal information coefficient C_M at different locations z for gravity levels $G = 0.7$, 1, and 1.5. (b) Surface plot of C_M as a function of G at different z.

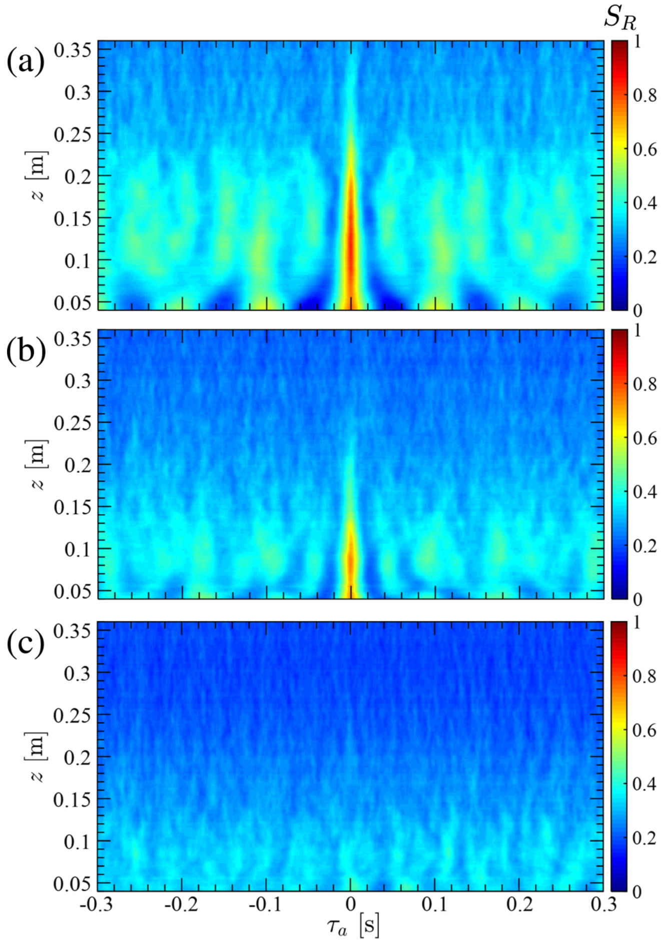

FIG. 5. Variation in the recurrence rate S_R of the SRPs as a function of the delay time τ_a at different locations z. (a) $G = 0.7$, (b) $G = 1$, and (c) $G = 1.5$.

reasonably corresponds to that of R_R, which supports the findings on the synchronized states obtained from the recurrence rate in the CRPs. Figure 5 shows the variation in S_R as a function of G and τ_a at different z. Note that τ_a corresponds to the actual delay time ($= \tau_l \Delta t$, where Δt is the time resolution of M_{w1} and M_{w2}). S_R at $\tau_a = 0$ takes high values at $z \sim 0.12$ m under the low gravity of $G = 0.7$, indicating that the dynamic behaviors of M_{w1} and M_{w2} exhibit synchronization without a time lag. S_R appears to change periodically in terms of τ_a with a frequency of approximately 20 Hz at $z \sim 0.12$ m. The frequency corresponds nearly to the dominant frequency of flame front oscillations in the near field driven by the periodic formation of toroidal vortex rings [see Fig. 8(A)], indicating the possible coexistence of the in-phase and antiphase states between M_{w1} and M_{w2}. S_R at $\tau_a = 0$ starts to decrease in the intermittent luminous zone ($z \geqslant 0.2$ m), and the completely synchronized state switches to the partially synchronized state in the far field ($z \geqslant 0.3$ m). The formation region of high S_R at $\tau_a = 0$ shrinks as G is increased to $G = 1$. It vanishes under the high gravity of $G = 1.5$ through its transition to the nonsynchronized state. The variation in S_R at $\tau_a = 0$ is shown in Fig. 6 as a function of G at different z. S_R takes high values in the near field under low gravity. It significantly decreases with increasing G. The distribution of S_R in terms of z and G nearly corresponds to that of R_R. The results in Figs. 2–6 clearly show that the nearly completely synchronized state between M_{w1} and M_{w2} in the near field changes to the partially synchronized state in the far field under low gravity, whereas both synchronized states vanish under high gravity.

Figure 7 shows the correlation coefficient C between the predicted values and the corresponding reference values of M_{w2} as a function of z for different G. C at $G = 0.7$ is approximately 0.95 for $z \leqslant 0.13$ m, showing the high pre-

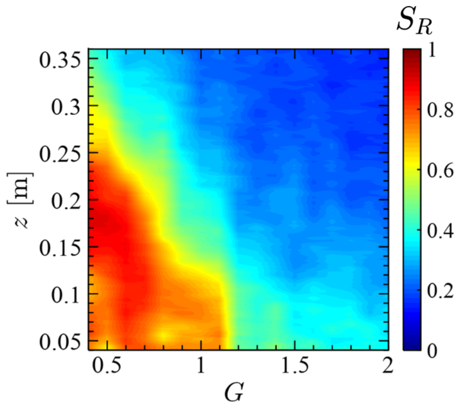

FIG. 6. Variation in the recurrence rate S_R of the SRPs as a function of gravity level G at different locations z. Here, $\tau_a = 0$.

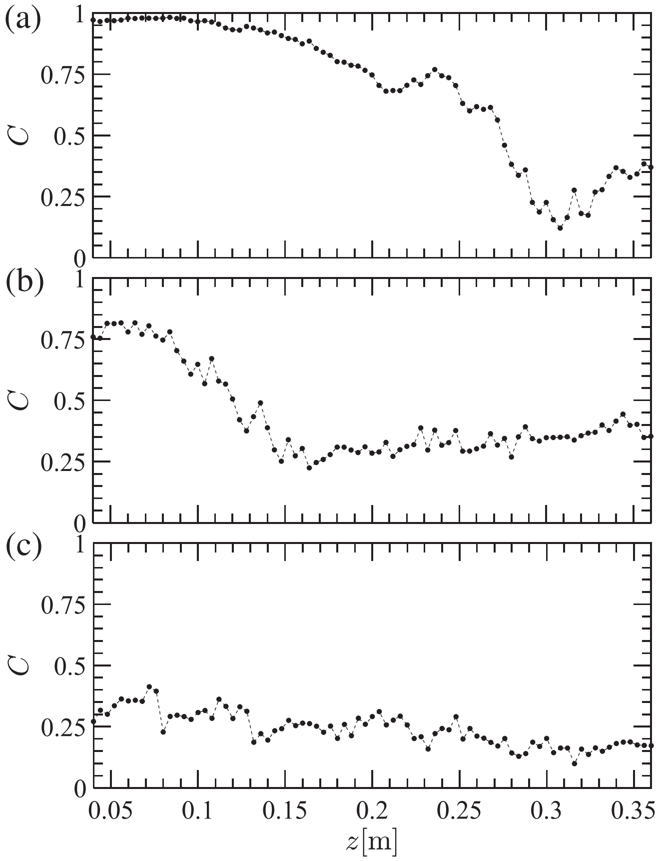

FIG. 7. Variation in the correlation coefficient C between the predicted values and the corresponding reference values of the second-order moment of flow velocity fluctuations M_{w2} at different locations z. (a) $G = 0.7$, (b) $G = 1$, and (c) $G = 1.5$.

dictability of M_{w2} in the near field. C monotonically decreases with increasing z. An important point to note here is that the high-C region corresponds reasonably well to R_R [see Fig. 3(a)], which provides strong evidence of the formation of the nearly completely synchronized state under low gravity. C at $G = 1$ starts to decrease at a lower location of $z = 0.08$ m compared with that at $G = 0.7$ and is approximately 0.3 at $z \leqslant 0.2$ m. In contrast, C at $G = 1.5$ takes low values at any z. The notable decrease in the predictability of M_{w2} is associated with the expansion of the formation region of high-dimensional chaos. These results show that the prediction of the second-order moment of flow velocity fluctuations by reservoir computing is useful for discussing the significant change in the synchronized state of two coupled turbulent diffusion flames covering from low to high gravity. Jiang and Lai [65] have applied reservoir computing to predict high-dimensional chaos in the Kuramoto-Sivashinsky equation, which describes the nonlinear dynamics of a propagating flame front. They provided an important insight into the setting of the spectral radius of the reservoir to markedly enhance the accuracy of the short-term prediction of high-dimensional chaos. Zhang *et al.* [66] have shown that reservoir computing can achieve the long-term prediction of the phase synchronization of low-dimensional chaos produced by coupled Rössler oscillators. In contrast, referring to recent studies [59,60], we studied the prediction accuracy as a function of the leaking rate of the reservoir to discuss the dynamical properties of the synchronized state. As shown in Fig. 7, the obtained distribution of the correlation coefficient between the actual and predicted second-order moments of flow velocity fluctuations in terms of the vertical location at different gravitational levels can reasonably explain the significant change from nearly complete synchronization in the near field to partial synchronization in the far field. The formula of the reservoir state $\mathbf{r}(t_i)$ in this paper differs from that used by Jiang and Lai [65] and Zhang *et al.* [66], but their approach will be important in our next study to obtain higher prediction accuracy of the spatiotemporal dynamics in two coupled buoyancy-induced turbulent flames.

We here discuss the physical mechanisms of the formation of the nearly complete synchronization in the near field, the partial synchronization in the far field under low gravity, and the disappearance of these synchronized states under high gravity, focusing on the vortical structures in two coupled turbulent diffusion flames. Figure 8 shows the temporal evolution of the vorticity field on the x-z plane at $G = 0.7$ and 1.5. The organized toroidal vortex rings with a plume neck are clearly formed at $z \sim 0.1$ m under the low gravity of $G = 0.7$. The formation of the asymmetric toroidal vortex rings along the centerline of the two flame sources is attributed to a modified Kelvin-Helmholtz-type hydrodynamic instability mechanism and the Rayleigh-Taylor instability mechanism. The asymmetric toroidal vortex rings are periodically produced in the continuous flame zone. The periodic formation of the asymmetric toroidal vortex rings has a significant impact on the emergence of nearly complete synchronization. The traveling toroidal vortex rings in the downstream direction merge and interact with each other at $z \geqslant 0.2$ m. Note that an intermittent luminous zone is formed at $0.2 \leqslant z \leqslant 0.25$ m. The coalescence and breakdown of the vortices with strong mutual interactions occur in the far field ($z \geqslant 0.3$ m), accompanied by the rapid spread of a turbulent-like plume. This enhances the irregularity of flow velocity fluctuations. As a result, the nearly completely synchronized state changes to a partially synchronized state in the far field under low gravity. Complex vortical structures with various scales and strengths are produced under the high gravity of $G = 1.5$. This is strongly associated with the formation of the nonsynchronized state. We here provide an additional interpretation of the synchronized states under low gravity from the viewpoint of the edge of chaos [67]. In accordance with the concept of the edge of chaos, low-dimensional chaos with regular spatial vortical structures corresponds to a laminar regime, whereas high-dimensional chaos with strong spatiotemporal irregularity corresponds to a turbulent regime. This implies that a significant transition from nearly complete synchronization to partial synchronization appears at a laminar-turbulent boundary in two coupled buoyancy-induced turbulent flames. For large-scale turbulent fire systems [68,69], the formation of more complex transverse vortical rings is promoted in the near field as the result of the rapid growth of buoyancy-driven Kelvin-Helmholtz hy-

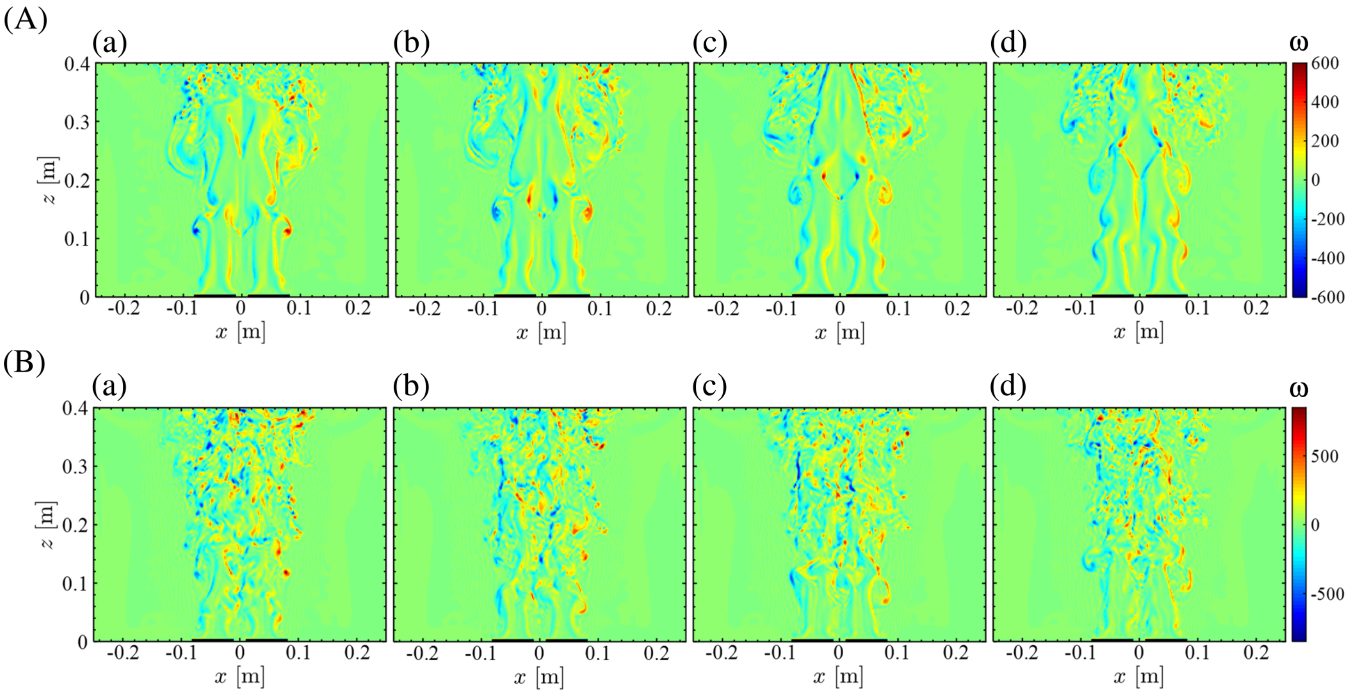

FIG. 8. Temporal evolution of the vorticity field on the x-z plane at $y = 0$ mm under (A) low gravity ($G = 0.7$) and (B) high gravity ($G = 1.5$). (a) $t = 2$ s, (b) $t = 2.025$ s, (c) $t = 2.05$ s, and (d) $t = 2.075$ s.

drodynamic and Rayleigh-Taylor instabilities. The nonlinear interaction of these vortical rings produces irregularity of the flow velocity fluctuations that are greater than that in this study, which leads to the disappearance of the nearly complete synchronization in the near field. This was clearly identified in the case of normal gravity using CRPs [46] but can be potentially explained by reservoir computing. Many experimental and numerical studies [37–45] have recently revealed the presence of two distinct classes of synchronization modes, in-phase synchronization, and antiphase synchronization in oscillators composed of arrays of laminar diffusion flames, providing the physical mechanisms behind the formation of in-phase and antiphase synchronizations. However, in those previous studies [37–45], the synchronization phenomena in two coupled turbulent flames under various gravity levels were not explored. Our findings will provide an encompassing understanding and interpretation of synchronization phenomena in buoyancy-induced turbulent diffusion flames in light of the gravity effect.

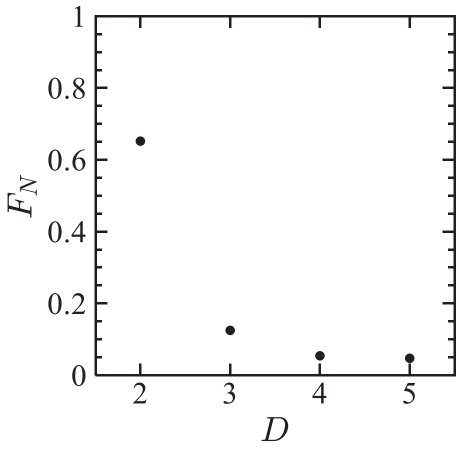

FIG. 9. Variation in the fraction F_N of false nearest neighbors of the trajectories in phase space as a function of the embedding dimension D.

IV. SUMMARY

We have numerically examined the synchronization phenomena of two coupled buoyancy-induced turbulent flames under various gravity levels by recurrence-based analysis and machine learning. We have used CRPs, SRPs, and reservoir computing. The most interesting discovery is a significant change from the nearly completely synchronized state in the near field to the partially synchronized state in the far field under low gravity. The periodic formation of asymmetric toroidal vortex rings plays an important role in the emergence of nearly complete synchronization. The traveling toroidal vortex rings substantially merge and interact with each other. The occurrence of the coalescence and breakdown of the vortices with strong mutual interaction enhances the irregularity of flow velocity fluctuations in the far field, resulting in the transition to a partially synchronized state. The synchronized states are gradually lost with increasing gravity level and finally become nonsynchronized states owing to the formation of complex vortical structures of various scales and strengths.

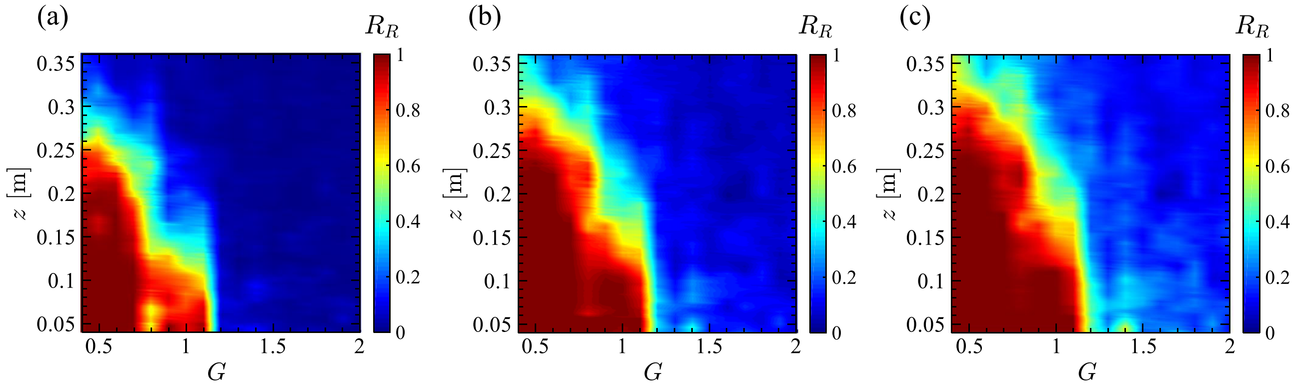

FIG. 10. Variations in the recurrence rate R_R of the CRPs as functions of vertical location z and gravitational level G at different recurrence point densities r_d. (a) $r_d = 0.01$, (b) $r_d = 0.05$, and (c) $r_d = 0.1$.

ACKNOWLEDGMENTS

This research was partially supported by the Private University Research Branding Project (Project No. 2017-2021) from the Ministry of Education, Culture, Sports, Science.

APPENDIX

The false nearest-neighbors method [56] is in widespread use for optimizing the embedding dimension of a phase space. In this paper, we set the embedding dimension by computing the ratio F_N $(=\sqrt{\frac{{d_{D+1}}^2-{d_D}^2}{{d_{D+1}}^2}})$ of the Euclidean distances between the position vectors in $(D+1)$- and D-dimensional phase spaces. Here, $d_D(=\|\mathbf{M}_{w1} - \mathbf{M}_{w1,n}\|)$ is the Euclidean distance between $\mathbf{M}_{w1}$ and its nearest-neighbor vector $\mathbf{M}_{w1,n}$ in the D-dimensional phase space. The variation in F_N as a function of D is shown in Fig. 9. Note that M_{w1} at $z = 0.1$ m under $G = 1$ is analyzed as a representative case. F_N is lower than 0.1 when $D \geqslant 4$, indicating that $D \geqslant 4$ is a suitable embedding dimension for the construction of the phase space. For the choice of the permutation patterns in a time series, the number of data points of the time series should be set to be sufficiently larger than $D!$. In our preliminary test, we found that the missing permutation patterns appear at $D = 7$ even in stochastic dynamics with a sufficient number of data points $(= 100\,000)$, such as Brownian motion. On the basis of the finding obtained by Kulp and Zunino [70], $D \leqslant 6$ should be considered to construct the SRPs. In contrast, the number of permutation patterns at $D = 4$ is $4!$ $(= 24)$, which is insufficient for capturing the complex dynamics of high-dimensional spatiotemporal chaos in a well-developed turbulent flow. Therefore, we set $D = 5$ in this paper.

Figure 10 shows the variations in R_R of the CRPs as functions of z and G at different recurrence point densities r_d. The distributions of R_R in terms of z and G do not significantly change at $0.05 \leqslant r_d \leqslant 0.1$. On this basis, we set r_d to 0.05 for the construction of the CRPs. Figure 11 shows the variations in the recurrence rate S_R of the SRPs as functions of z and G at different τ. The distributions of S_R in terms of z and G do not significantly change at $5 \leqslant \tau \leqslant 10$. On this basis, τ is set to 5 for the construction of the SRPs.

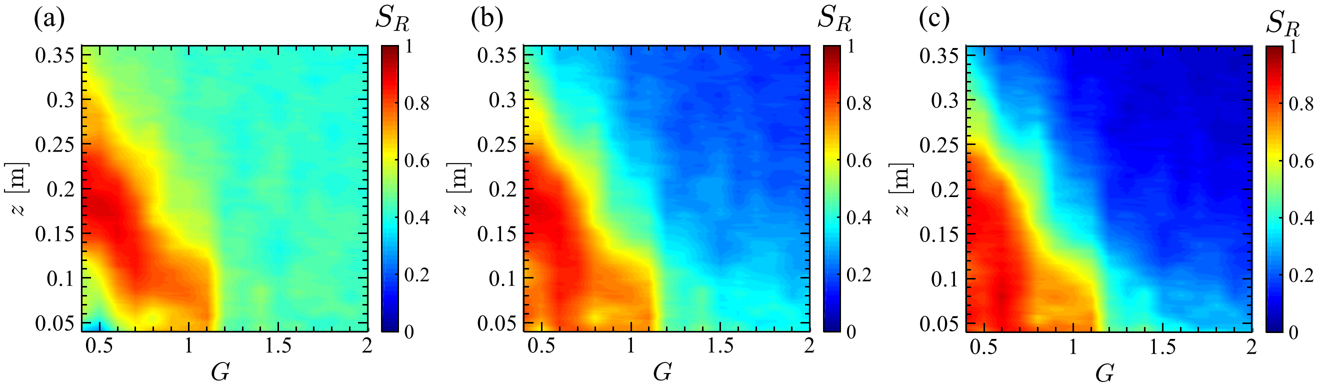

FIG. 11. Variations in the recurrence rate S_R of the SRPs as functions of vertical location z and gravitational level G at different embedding delay times τ. (a) $\tau = 1$, (b) $\tau = 5$, and (c) $\tau = 10$.

[1] L. D. Chen, J. P. Seaba, W. M. Roquemore, and L. P. Goss, Proc. Combust. Inst. **22**, 677 (1989).

[2] V. R. Katta and W. M. Roquemore, Combust. Flame **92**, 274 (1993).

[3] H. Gotoda, S. Kawaguchi, and Y. Saso, Exp. Therm. Fluid Sci. **32**, 1759 (2008).

[4] A. F. Ghoniem, I. Lakkis, and M. Soteriou, Proc. Combust. Inst. **26**, 1531 (1996).

[5] D. Drysdale, *An Introduction to Fire Dynamics* (Wiley, New York, 1994).

[6] B. M. Cetegen and K. D. Kasper, Phys. Fluids **8**, 2974 (1996).

[7] E. J. Weckman and A. B. Strong, Combust. Flame **105**, 245 (1996).

[8] S. R. Tieszen, T. J. O'Hern, R. W. Schefer, E. J. Weckman, and T. K. Blanchat, Combust. Flame **129**, 378 (2002).

[9] S. R. Tieszen, T. J. O'Hern, E. J. Weckman, and R. W. Schefer, Combust. Flame **139**, 126 (2004).

[10] P. E. DesJardin, T. J. O'Hern, and S. R. Tieszen, Phys. Fluids **16**, 1866 (2004).

[11] Y. Xin, J. P. Gore, K. B. McGrattan, R. G. Rehm, and H. R. Baum, Combust. Flame **141**, 329 (2005).

[12] Y. Xin, S. A. Filatyev, K. Biswas, J. P. Gore, R. G. Rehm, and H. R. Baum, Combust. Flame **153**, 499 (2008).

[13] R. W. Davis, E. F. Moore, W. M. Roquemore, L. D. Chen, V. Vilimpoc, and L. P. Goss, Combust. Flame **83**, 263 (1991).

[14] H. Sato, G. Kushida, K. Amagai, and M. Arai, Proc. Combust. Inst. **29**, 1671 (2002).

[15] W. E. Mell, K. B. McGrattan, and H. R. Baum, Proc. Combust. Inst. **26**, 1523 (1996).

[16] X. Zhou, K. H. Luo, and J. J. R. Williams, Combust. Flame **129**, 11 (2002).

[17] A. Hamins, J. C. Yang, and T. Kashiwagi, Proc. Combust. Inst. **24**, 1695 (1992).

[18] B. M. Cetegen and T. A. Ahmed, Combust. Flame **93**, 157 (1993).

[19] B. M. Cetegen, Y. Dong, and M. C. Soteriou, Phys. Fluids **10**, 1658 (1998).

[20] B. M. Cetegen and Y. Dong, Exp. Fluids **28**, 546 (2000).

[21] L. Hu, J. Hu, and J. L. de Ris, Combust. Flame **162**, 1095 (2015).

[22] H. Abe, A. Ito, and H. Torikai, Proc. Combust. Inst. **35**, 2581 (2015).

[23] H. Gotoda, K. Michigami, K. Ikeda, and T. Miyano, Combust. Theory Model. **14**, 479 (2010).

[24] H. Gotoda, M. Amano, T. Miyano, T. Ikawa, K. Maki, and S. Tachibana, Chaos **22**, 043128 (2012).

[25] J. Tony, E. A. Gopalakrishnan, E. Sreelekha, and R. I. Sujith, Phys. Rev. E **92**, 062902 (2015).

[26] R. Sampath and S. R. Chakravarthy, Combust. Flame **172**, 309 (2016).

[27] H. Gotoda, H. Kobayashi, and K. Hayashi, Phys. Rev. E **95**, 022201 (2017).

[28] Y. Guan, M. Murugesan, and L. K. B. Li, Chaos **28**, 093109 (2018).

[29] C. Aoki, H. Gotoda, S. Yoshida, and S. Tachibana, J. Appl. Phys. **127**, 224903 (2020).

[30] L. Zunino, M. C. Soriano, and O. A. Rosso, Phys. Rev. E **86**, 046210 (2012).

[31] K. Takagi, H. Gotoda, I. T. Tokuda, and T. Miyano, Phys. Rev. E **96**, 052223 (2017).

[32] K. Takagi, H. Gotoda, I. T. Tokuda, and T. Miyano, Phys. Lett. A **382**, 3181 (2018).

[33] T. Tokami, T. Hachijo, T. Miyano, and H. Gotoda, Phys. Rev. E **101**, 042214 (2020).

[34] Y. Kuramoto, *Chemical Oscillations, Waves, and Turbulence* (Springer, Berlin, 1984).

[35] I. Z. Kiss, Y. Zhai, and J. L. Hudson, Science **296**, 1676 (2002).

[36] A. Pikovsky, M. Rosenblum, and J. Kurths, *Synchronization* (Cambridge University Press, Cambridge, U.K., 2001).

[37] H. Kitahata, J. Taguchi, M. Nagayama, T. Sakurai, Y. Ikura, A. Osa, Y. Sumino, M. Tanaka, E. Yokoyama, and H. Miike, J. Phys. Chem. A **113**, 8164 (2009).

[38] D. M. Forrester, Sci. Rep. **5**, 16994 (2015).

[39] K. Okamoto, A. Kijima, Y. Umeno, and H. Shima, Sci. Rep. **6**, 36145 (2016).

[40] K. Mochizuki, T. Matsuoka, and Y. Nakamura, Bull. Jpn. Assoc. Fire Sci. Eng. **67**, 77 (2017).

[41] K. Manoj, S. A. Pawar, and R. I. Sujith, Sci. Rep. **8**, 11626 (2018).

[42] S. Dange, S. A. Pawar, K. Manoj, and R. I. Sujith, AIP Adv. **9**, 015119 (2019).

[43] T. Chen, X. Guo, J. Jia, and J. Xiao, Sci. Rep. **9**, 342 (2019).

[44] T. Yang, X. Xia, and P. Zhang, Phys. Rev. Fluids **4**, 053202 (2019).

[45] N. Fujisawa, K. Imaizumi, and T. Yamagata, Exp. Therm. Fluid Sci. **110**, 109924 (2020).

[46] K. Takagi, H. Gotoda, T. Miyano, S. Murayama, and I. T. Tokuda, Chaos **28**, 045116 (2018).

[47] N. Marwan and J. Kurths, Phys. Lett. A **302**, 299 (2002).

[48] N. Marwan, M. C. Romano, M. Thiel, and J. Kurths, Phys. Rep. **438**, 237 (2007).

[49] M. V. Caballero-Pintado, M. Matilla-García, and M. Ruiz Marín, Chaos **28**, 063112 (2018).

[50] A. Groth, Phys. Rev. E **72**, 046220 (2005).

[51] J. Pathak, Z. Lu, B. R. Hunt, M. Girvan, and E. Ott, Chaos **27**, 121102 (2017).

[52] J. Pathak, B. Hunt, M. Girvan, Z. Lu, and E. Ott, Phys. Rev. Lett. **120**, 024102 (2018).

[53] K. B. McGrattan, H. R. Baum, R. G. Rehm, A. Hamins, and G. P. Forney, Fire dynamics simulator-Technical reference guide, National Institute of Standards and Technology, Report No. NISTIR6467, 2000 (unpublished).

[54] K. B. McGrattan, Fire dynamics simulator (version 4)-Technical reference guide, National Institute of Standards and Technology, NIST Special Publication Report No. 1018, 2006 (unpublished).

[55] C. Bandt and B. Pompe, Phys. Rev. Lett. **88**, 174102 (2002).

[56] M. B. Kennel, R. Brown, and H. D. I. Abarbanel, Phys. Rev. A **45**, 3403 (1992).

[57] A. M. Fraser and H. L. Swinney, Phys. Rev. A **33**, 1134 (1986).

[58] A. Shinozaki, T. Miyano, and Y. Horio, Nonlin. Theor. Appl. **11**, 466 (2020).

[59] T. Weng, H. Yang, C. Gu, J. Zhang, and M. Small, Phys. Rev. E **99**, 042203 (2019).

[60] F. O. Mannan, M. Jarvela, and K. Leiderman, Phys. Rev. E **102**, 033114 (2020).

[61] M. Lukoševičius, in *Neural Networks: Tricks of the Trade* (Springer, Berlin, 2012), pp. 659–686.

[62] A. N. Tikhonov and V. Y. Arsenin, *Solutions of Ill Posed Problems* (Winston and Sons, Washington, D.C., 1977).

[63] K. Takagi and H. Gotoda, Phys. Rev. E **98**, 032207 (2018).

[64] H. Kobayashi, H. Gotoda, and S. Tachibana, Physica A **510**, 345 (2018).

[65] J. Jiang and Y.-C. Lai, Phys. Rev. Research **1**, 033056 (2019).

[66] C. Zhang, J. Jiang, S.-X. Qu, and Y.-C. Lai, Chaos **30**, 083114 (2020).

[67] Y-C. Lai and T. Tél, *Transient Chaos*, Springer Series on Applied Mathematical Sciences Vol. 173 (Springer, Berlin, 2010).

[68] J. G. Quintiere, *Fundamentals of Fire Phenomena* (Wiley, Hoboken, NJ, 2006).

[69] W. Thurston, J. D. Kepert, K. J. Tory, and R. J. B. Fawcett, Int. J. Wildland Fire **26**, 317 (2017).

[70] C. W. Kulp and L. Zunino, Chaos **24**, 033116 (2014).